Journal of Power Sources 613 (2024) 234857

Contents lists available at ScienceDirect

Journal of Power Sources

journal homepage: www.elsevier.com/locate/jpowsour

Development and calibration of a fast flow model for solid oxide cell stack internal manifolds

Oscar Furst, Olaf Deutschmann *

Karlsruhe Institute of Technology, Kaiserstraße 12, Karlsruhe, 76131, Baden-Württemberg, Germany

HIGHLIGHTS

- Commonly used Darcy–Weisbach friction factor shown to be inaccurate in SOC manifolds.
- Pressure loss coefficient expressions for junctions in SOC manifolds are provided.
- Fast and accurate algebraic model of the flow distribution in SOC stacks is presented.

GRAPHICAL ABSTRACT

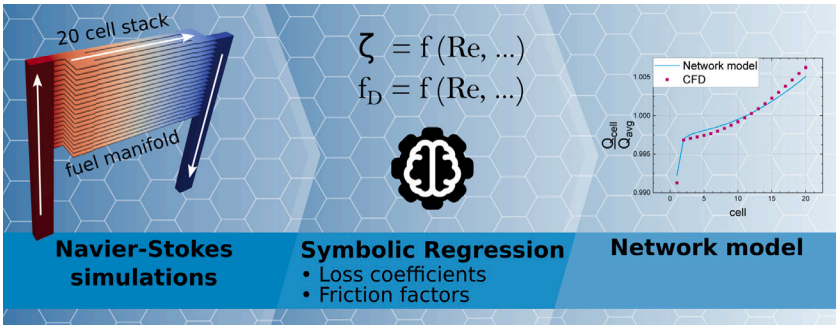

ARTICLE INFO

Keywords:
Solid oxide cell stack internal manifold
Flow network model
Pressure loss coefficients

ABSTRACT

Due to the commercialization of solid oxide cells (SOC) progressing at an accelerated pace, computationally inexpensive SOC models adapted to the iterative nature of the engineering process are in increasing demand. Flow simulation in the stack is especially challenging in this regard because detailed computational fluid mechanic models are computationally demanding, while simplified models rely on pressure loss coefficients and friction factors not readily available in the literature. In this study, a computationally inexpensive algebraic model of an SOC stack internal manifold is developed and calibrated for laminar flow conditions. Thereby, pressure loss coefficients and Darcy friction factors are determined for a broad range of operating conditions through symbolic regression of Navier–Stokes flow simulation results of stacks of 20 to 40 cells. The derived Darcy friction factors for the inlet and outlet manifolds prove to be of particular importance, as they deviate strongly from the expressions assumed in similar modeling studies. The predictive power of the developed model is demonstrated by providing accurate predictions of the flow distribution in the stack, even outside of the calibration window.

1. Introduction

In recent years, the commercialization of solid oxide cells (SOC) has experienced an unprecedented surge, with the production capabilities of commercial manufacturers being scaled up to meet the anticipated global demand [1]. Concurrently, the planning of industrial applications of large quantities of integrated SOC stacks [2,3] drives the demand for simulation tools adapted to the optimization tasks performed during the system engineering process [4]. While SOC models have traditionally served as valuable academic tools for comprehending the intricate physico-chemical dynamics within cells and stacks, this change necessitates the development of faster simulation tools tailored to the iterative nature of the engineering process.

* Corresponding author.
E-mail addresses: oscar.furst@kit.edu (O. Furst), deutschmann@kit.edu (O. Deutschmann).
URL: https://www.itcp.kit.edu/deutschmann/ (O. Deutschmann).

https://doi.org/10.1016/j.jpowsour.2024.234857
Received 10 April 2024; Received in revised form 27 May 2024; Accepted 3 June 2024
Available online 26 June 2024

Nomenclature

Abbreviations

BC	Boundary condition
GCI	Grid convergence index
MEA	Membrane electrode assembly
NRMSD	Normalized root mean square deviation
SOC	Solid oxide cell

Sub- and superscripts

i	i^{th} cell (counting from the top)
n	n^{th} cell (counting from the top)
avg	Average
B	Bend
C	Common branch (of a tee junction)
in	Inlet
M	Manifold
out	Outlet
S	Side branch (of a tee junction)
St	Straight passage (of a tee junction)
tot	Total

Variables

μ	[Pa s]	Dynamic viscosity
ν	[$m^2\,s^{-1}$]	Kinematic viscosity
ρ	[$kg\,m^{-3}$]	Density
ζ	[–]	Pressure loss coefficient
a		Slope of a linear function
b		Intersect of a linear function
D_H	[m]	Hydraulic diameter
f_D	[–]	Darcy friction factor
h	[m]	Height
k	[m^2]	Permeability
L	[m]	Length
n	[–]	Number of cells in the stack
p	[Pa]	Pressure
Q	[$m^3\,s^{-1}$]	Flow rate
Re	[–]	Reynolds number
u	[$m\,s^{-1}$]	Velocity
x, y, z	[m]	Spacial coordinates

Models used to optimize cell and stack designs need to simulate the system performance as a function of various design parameters such as cell materials, electrode microstructure and operating conditions. By nature, the cell models used for such tasks need to be extrapolatable with reasonable accuracy beyond the operating points used for calibration, which is achieved through detailed but computationally expensive modeling of the underlying physical processes. Fortunately, such simulations can be expedited through the use of space-marching [5] and clustering algorithms [6]. The computational efficiency of flow simulation within the stack, however, emerges as a critical factor. The intricacies of computational fluid mechanic models that encompass both inertial and viscous flow patterns, along with their impact on flow distribution in the stack, pose a significant computational challenge. Simultaneously, flow maldistribution caused by the stack manifold can have a significant effect on stack operating conditions, especially regarding degradation rates [7]. Such effects are especially relevant whenever a limited amount of space can be allotted to the manifold system, as is the case for mobile applications [8]. In light of this, there is a growing imperative to develop stack manifold models that strike a balance between accuracy and computation time, facilitating the swift progression of the design and optimization processes.

The flow distribution in stacks can be studied with high accuracy using 3-dimensional stack models resolving the flow-field with the Navier–Stokes equation [9]. Compared to the experimental approach, detailed simulations have the added advantage of providing access to the entire flow-field. However, such models suffer from long computation times, especially when the electrochemistry is also simulated.

In order to reduce computational costs, Beale et al. [10–12] introduced the distributed resistance analogy for solid oxide fuel cell manifold modeling. With this method, the full momentum conservation equation is still solved in the manifold, but simplified inside the active region of the stack, which allows the use of a coarser mesh. In exchange for a minimal loss in precision, computation times can be reduced by roughly an order of magnitude.

The most computationally efficient models are flow network models [13–15], because they only require the solution of a set of algebraic equations. While the loss of accuracy is greater, sub-second computation times can be achieved, which is a reduction by more than four orders of magnitude compared to the detailed simulation. However, their accuracy relies heavily on the availability of pressure loss coefficients for the geometric features of the studied manifold, such as junctions and bends. This is especially challenging for stack manifolds because the literature on pressure loss coefficients in tee junctions focuses heavily on turbulent operation [16], leading scientists to use ill-suited coefficients or neglect them altogether [13,17]. In any stack, the final portion of the inlet manifold and the initial portion of the outlet manifold operate in the laminar regime due to the low flow rate. In stacks with low flow rates at the inlet (e.g., due to a low number of cells), and therefore low Reynolds number, the flow can be fully laminar.

In this study, a network model is developed for the manifold design of interest, for which pressure loss coefficients are computed using 3-dimensional Navier–Stokes flow simulation results obtained from stacks comprising 20 to 40 cells under laminar flow conditions. The use of symbolic regression is showcased for the development of closed-form expressions used for the computation of loss coefficients in the simplified model.

Expressions for the evaluation of the Darcy friction factor in the inlet and outlet manifolds are also developed, and the result is shown to differ from the friction factors often used in similar modeling studies.

The resulting model is shown to predict flow maldistribution in the studied manifold geometry with good accuracy and negligible computation times. Crucially, the model demonstrates its efficacy beyond the confines of the calibration window, underlining its potential as a valuable tool for engineers and researchers engaged in the design and optimization of SOC systems. Compared to detailed, three-dimensional computational fluid dynamics (CFD) investigations, this approach can be leveraged to expedite the simulations of full SOC stacks with internal manifolds.

2. Methodology

2.1. Manifold geometry

For the purpose of this study, a U-type stack manifold design was developed for the stacks of 9 cm × 14.2 cm fuel electrode-supported cells under co-flow operation studied by Wehrle et al. [18]. Literature on current commercial stack manifold designs is very scarce, with the notable exception of the Jülich Mark-F which is a counter-flow design [10,19,20]. Therefore, the design produced herein resulted from the aggregation of geometric data from similar modeling studies [21,22] and educated guesses based on published images of commercial stacks [23,24]. In this study, the modeling efforts are focused on the

Table 1
Fuel manifold geometry parameters.

Parameter	Value	Unit
Manifold channel width	17	mm
Manifold channel depth	17	mm
Fuel channel width	4.75	mm
Fuel channel height	1	mm
Fuel channel length	90	mm
Inlet & outlet header length	17	mm
Sealing width	8	mm
Interconnect rib width	1.5	mm
Interconnect total height	3.5	mm
MEA height	0.4103	mm

(a) Schematic of the flow paths through the fuel channels of a cell.

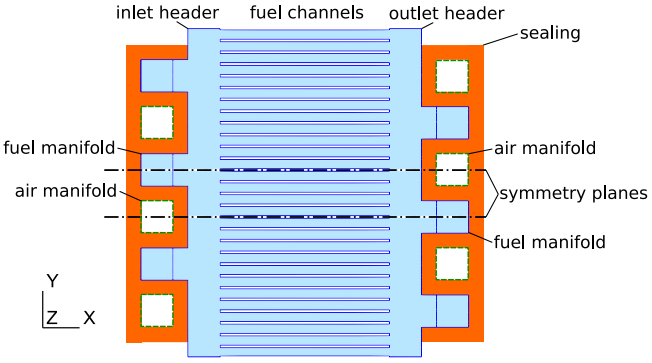

(b) Simulated flow domain for a 20 cell stack, corresponding to the region demarcated by symmetry planes. Annotations in italic correspond to boundary conditions listed in Table 2.

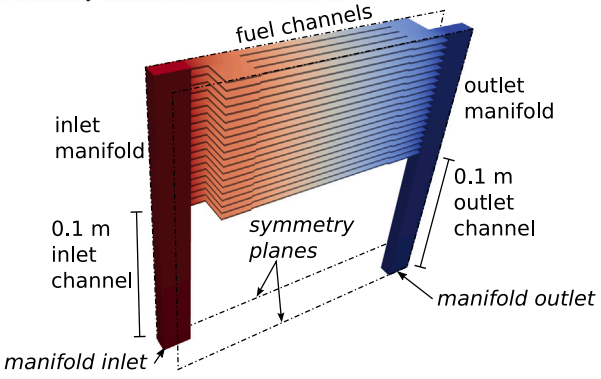

Fig. 1. Visualizations of the geometry of the simulated manifold.

fuel manifold, as the symmetrical design allows to apply the results to the air manifold as well. A schematic of the resulting fuel manifold for a single cell is shown in Fig. 1(a) and a detailed list of measurements is provided in Table 1.

Due to the repetitive structure of the flow domain, the computational cost of detailed simulations can be greatly reduced by simulating a slice of the manifold with symmetry boundary conditions on each side, as shown in Fig. 1(b). Due to the large width of the stack (142 mm) compared to the slice (25 mm), the incurred loss of accuracy is expected to be small.

2.2. Navier–Stokes flow model

The flow in the manifold was studied through simulations using the SimpleFOAM solver of OpenFOAM [25], which solves the steady-state incompressible Navier–Stokes equations using the SIMPLE algorithm. In this case, the following set of the equations is solved [26]:

$$\nabla \cdot u = 0 \tag{1}$$

Table 2
Boundary conditions used to solve the Navier–Stokes equation.

Boundary	Velocity BC	Pressure BC
Manifold inlet	parabolic profile, $\bar{u} = u_{\text{in}}$	$\frac{\partial p}{\partial n} = 0$
Manifold outlet	$\frac{\partial u}{\partial n} = 0$	$p = 0$
Symmetry plane	symmetry	symmetry
Walls	$u = 0$	$\frac{\partial p}{\partial n} = 0$

Table 3
List of simulations, each characterized by the number of cells in the stack and the average flow velocity in the fuel channels $\bar{u}_{\text{cells}}$, leading to a Reynolds number Re_{in} at the inlet.

n°	Number of cells	$\bar{u}_{\text{cells}}$	Re_{in}	Function
1	40	$1\,\text{m}\,\text{s}^{-1}$	284	Training data
2	20	$1\,\text{m}\,\text{s}^{-1}$	142	Training data
3	20	$2\,\text{m}\,\text{s}^{-1}$	248	Training data
4	20	$0.5\,\text{m}\,\text{s}^{-1}$	71	Training data
5	20	$3\,\text{m}\,\text{s}^{-1}$	426	Test data
6	20	$0.25\,\text{m}\,\text{s}^{-1}$	47	Validation data

$$\nabla \cdot (u \otimes u) = \nabla \cdot R - \nabla \frac{p}{\rho} \tag{2}$$

with the velocity vector u, the stress tensor R and the kinematic pressure $\frac{p}{\rho}$.

The boundary conditions (BC) used for the simulations are listed in Table 2. Inlet and outlet channels with a length of 0.1 m were added to the geometry in order to guarantee a fully developed flow at the inlet of the manifold and reduce the influence of the outlet boundary conditions on the flow in the outlet manifold.

In order to analyze the flow over a broad range of parameters, the flow was simulated for stacks with a different number of cells (20 to 40) and for a range of Reynolds numbers ($Re_{\text{in}} \in \{47, 71, 142, 284, 426\}$). At a Reynolds number of 568 achieved with an average fuel channel velocity $\bar{u}_{\text{cells}} = 4\,\text{m}\,\text{s}^{-1}$ in the 20 cell stack, transient behavior was observed which cannot be resolved using the SimpleFOAM solver. Solving the transient Navier–Stokes equation for stacks of 20 cells and the level of accuracy targeted by this study is not practically feasible due to computation times increasing by several orders of magnitude. Therefore, the start of this transient flow regime represents an upper bound for the range of Reynolds numbers at the inlet that can be studied with the present methodology. Simulations were performed using the fluid properties of a 90% H_2O, 10% H_2 mixture at 650 °C, leading to a kinematic viscosity of $\nu = 3.15 \cdot 10^{-4}\,\text{m}^2\,\text{s}^{-1}$. An exhaustive list of investigated flow conditions is provided in Table 3.

In order to ensure that the flow model resulting from this study is not only applicable to the fitted flow conditions, the simulation with the highest Reynolds number was kept as test data and the simulation with the lowest Reynolds number was kept as validation data. The test data was not used to fit the loss coefficients developed in this study, but was consulted during their development in order to ensure accurate extrapolation beyond the calibration window. The validation data was used only to test the accuracy of the resulting model at the very end of the study.

The applicability of Reynolds' law of similarity to all quantities of interest in this study (pressure loss coefficients, Darcy friction factors, permeabilities and flow distribution) was confirmed by performing an additional simulation at $Re_{\text{in}} = 142$ with a kinematic viscosity of $\nu = 6.30 \cdot 10^{-4}\,\text{m}^2\,\text{s}^{-1}$, which led to discrepancies in the results well below 0.1% in magnitude. As a result, the findings of this study are not only applicable to flows with the simulated gas properties, but to any flow of similar Reynolds number.

A grid convergence study according to Roache [27] was performed on the 20 cells, $Re_{\text{in}} = 284$ case using 3 grids with respectively 18, 50 and 142 million hexahedral cells (grid refinement ratio $r \approx 1.4$). The difference in the average pressure in the inlet manifold and the outlet manifold Δp_{stack}, measured 1 mm below the first cell, was used as a

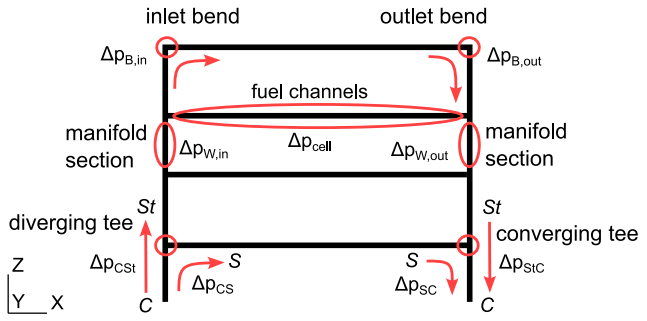

Fig. 2. Schematic of the manifold geometry with a visualization of flow features with significant influence on the total pressure in the flow. The nomenclature used to differentiate the common channel *C*, side channel *S* and straight passage *St* of converging and diverging tees is annotated in italic.

criterion for the computation of the relative error between two meshes

$$\epsilon_{12} = \frac{\Delta p_{\text{stack}}^{\text{grid 2}} - \Delta p_{\text{stack}}^{\text{grid 1}}}{\Delta p_{\text{stack}}^{\text{grid 1}}}. \tag{3}$$

Using second order interpolation and integration schemes in OpenFOAM, an order of convergence

$$p = \ln\left(\frac{\Delta p_{\text{stack}}^{\text{grid 1}} - \Delta p_{\text{stack}}^{\text{grid 2}}}{\Delta p_{\text{stack}}^{\text{grid 2}} - \Delta p_{\text{stack}}^{\text{grid 3}}}\right) / \ln(r) = 1.75 \tag{4}$$

and a grid convergence index

$$GCI = \frac{3\,|\epsilon_{12}|\,r^p}{(r^p - 1)} = 3.8\% \tag{5}$$

was computed for the intermediate mesh, which provides a reasonable error band for the solution. As the grid convergence study was performed over three meshes, the results could be verified to be in the asymptotic range of convergence. Results reported herein were all obtained using the intermediate grid spacing.

2.3. Computation of pressure losses

The following significant flow features in which total pressure $p_{\text{tot}} = p + \rho\,\vec{u}^2/2$ is lost or recovered are isolated in the simulated geometry (see Fig. 2):

- Diverging tees in the inlet manifold
- Converging tees in the outlet manifold
- Straight channel sections between tees
- Bends at the upper end of the manifolds
- Fuel channels, including inlet and outlet headers

The methodology used to compute the pressure gradients and loss coefficients in the manifolds is visualized in Fig. 3(a):

In order to assimilate the simulated results to a one-dimensional network model, the dimensionality of the results is reduced by averaging the static pressure $p(x, y, z)$, axial velocity $u_z(x, y, z)$ and total pressure $p_{\text{tot}}(x, y, z)$ across the cross-section of the manifolds in order to obtain $\overline{p}(z)$, $\overline{u}_z(z)$ and $\overline{p}_{\text{tot}}(z)$ which are only functions of the height coordinate.

For every manifold section located between the fuel channels of two cells, a linear regression is performed to express the total pressure in the i^{th} manifold section as a linear function of the manifold height

$$\overline{p}_{\text{tot}}(z) \approx a_i\, z + b_i \qquad z \in \left[z_{i,1/4}, z_{i,3/4}\right] \tag{6}$$

with the total pressure averaged over the cross section of the manifold $\overline{p}_{\text{tot}}$ expressed as a function of the height coordinate z, the slope a_i and intercept b_i determined through linear regression, knowing that the slope $a_i = \partial \overline{p}_{\text{tot}}^{\,i}/\partial z$ is the pressure gradient in the i^{th} manifold section.

Since the adjacent tee junctions causes a disturbance of the pressure in the nearby regions of the manifold sections (seen in the plot of $\overline{p}_{\text{tot}}(z)$ in Fig. 3(a)), the regression is only performed over half of the length of every section, from the coordinate $z = z_{i,1/4}$ to the coordinate $z = z_{i,3/4}$ which exclude the first and last quarter of the manifold sections.

At the inlet and outlet of the headers in the cells, the pressure is undisturbed by the adjacent junctions. Therefore, the total pressures at the start of the inlet header $\overline{p}^{\,i}_{\text{tot,cell,in}}$ and the end of the outlet header $\overline{p}^{\,i}_{\text{tot,cell,out}}$ are simply averaged over their cross-section:

$$\overline{p}^{\,i}_{\text{tot,cell,pos}} = \frac{1}{h_{\text{cell}}\, w_{\text{M}}} \int_{z_{i,\text{begin}}}^{z_{i,\text{end}}} \int_{y_{\text{begin}}}^{y_{\text{end}}} \overline{p}_{\text{tot}}(x_{\text{pos}}, y, z)\, dy\, dz$$
$$\text{with pos} \in \{\text{in}, \text{out}\} \tag{7}$$

with h_{cell} the height of a fuel channel, w_{M} the width of the manifold and its outlet towards the fuel channels, y_{begin} and $y_{\text{end}} = y_{\text{begin}} + w_{\text{M}}$ the y-coordinates of the sides of the manifold and $z_{i,\text{begin}}$ and $z_{i,\text{end}} = z_{i,\text{begin}} + h_{\text{cell}}$ the heights at which the ith fuel channel begins and ends. They are used to compute the pressure losses along the cells and the pressure loss coefficients of the tees and bends.

Herein, the nomenclature of Idelchik [16] was adopted to differentiate between the three branches of converging and diverging tees. The branch with the highest flow rate, which is the source of the flow in diverging tees and the sink of the flow in converging tees, is called the *common channel* and the subscript *C* is used. The branch opposite of the common channel is called the *straight passage* and the subscript *St* is used. The remaining branch is called the *side branch* and the subscript *S* is used.

Diverging tees have two flow paths: turning from the common channel to the side branch, and the straight passage from the common channel (see Fig. 2). Pressure loss due to friction is observed for the turning flow, while pressure recovery is observed for the straight passage (see Fig. 3(a)). The rise in total pressure across the junctions is due to low-speed gas from the boundary layer which exits the flow, which leaves the gas with a higher specific energy in the main channel [16]. The corresponding pressure loss coefficients are computed as follows [16]:

$$\zeta_{\text{CS}} = \frac{\overline{p}_{\text{tot,S}} - \overline{p}_{\text{tot,C}}}{\rho \overline{u}^2_{z,C}/2} \tag{8}$$

$$\zeta_{\text{CSt}} = \frac{\overline{p}_{\text{tot,St}} - \overline{p}_{\text{tot,C}}}{\rho \overline{u}^2_{z,C}/2}. \tag{9}$$

As previously mentioned and seen in Fig. 3(a), changes in total pressure due to this geometrical feature can already be observed in the manifold sections before and after the tees. In order to separate the effects of the wall friction from the effect of the tee, the total pressure drop is computed using the results of the linear regression:

$$\Delta p^i_{\text{CSt}} = \overline{p}^{\,i}_{\text{tot,St}} - \overline{p}^{\,i}_{\text{tot,C}}$$
$$= a_{i-1}\, z_{\text{i-1,begin}} + b_{i-1} - \left(a_i\, z_{\text{i,end}} + b_i\right). \tag{10}$$

The linear regression is not needed in the fuel channels, so that the turning pressure drop is computed as:

$$\Delta p^i_{\text{CS}} = \overline{p}^{\,i}_{\text{tot,cell,in}} - \overline{p}^{\,i}_{\text{tot,C}}$$
$$= \overline{p}^{\,i}_{\text{tot,cell,in}} - \left(a_i\, z_{\text{i,end}} + b_i\right). \tag{11}$$

In the converging tees of the outlet manifold, the two flow paths go from the side branch to the common branch and from the straight channel to the common branch (see Fig. 2). The same methodology as above is employed, with the pressure drops being computed in the direction of the flow:

$$\zeta_{\text{SC}} = \frac{\overline{p}_{\text{tot,C}} - \overline{p}_{\text{tot,S}}}{\rho \overline{u}^2_{z,C}/2} \tag{12}$$

$$\zeta_{\text{StC}} = \frac{\overline{p}_{\text{tot,C}} - \overline{p}_{\text{tot,St}}}{\rho \overline{u}^2_{z,C}/2}. \tag{13}$$

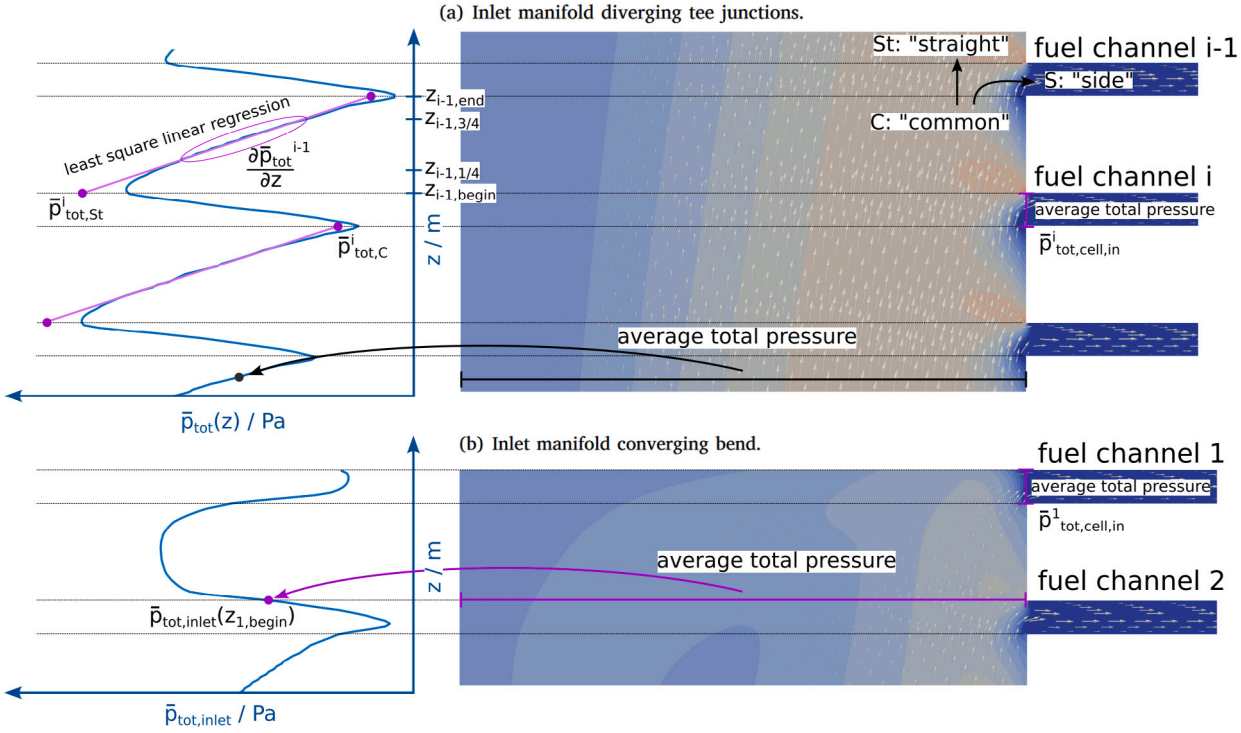

Fig. 3. Visualization of methodology used to compute (a) the pressure gradient along sections of the inlet manifold, pressure drops across tees and (b) the pressure drop across bends.

At the top of the stack, there is a converging bend from the inlet manifold to the uppermost cell and a diverging bend from the cell to the outlet manifold. These bends also have a significant influence on the total pressure profile in the uppermost manifold sections, as is shown in Fig. 3(b). Especially at the end of the inlet manifold, the stagnation of the flow causes an increase of the static pressure. The increased pressure causes a reversal of the flow direction in the low velocity parts of the manifold cross section, which leads to a large eddy. The eddy continually transports higher-energy gas, which is entrained by the relatively fast bulk flow, past the second fuel channel. Simultaneously, the other side of the eddy transports very slowly moving gas in the opposite direction over a much larger area. Due to the nonlinearity of the contribution of velocity to the kinetic energy, the eddy leads to an increase of the total pressure up to the middle of the final manifold section. After this point, the vertical motion of the eddy stops gradually, as its motion is mostly lateral in the uppermost part of the manifold. The increase in total pressure is further accentuated by the reversed flow outside of the symmetry plane (not visible on the figure), close to the lateral manifold walls, which leaves the manifold through the second fuel channel. This further removes slowly-moving portions of the flow, thereby increasing the energy of the flow per unit volume [16]. In order to capture this effect, the uppermost manifold section is included in the bend loss coefficients:

$$\zeta_{B,in} = \frac{\bar{p}^{1}_{tot,cell,in} - \bar{p}_{tot,inlet}\left(z_{1,begin}\right)}{\rho(\bar{u}_{z,inlet}(z_{1,begin}))^2/2} \tag{14}$$

$$\zeta_{B,out} = \frac{\bar{p}_{tot,outlet}\left(z_{1,begin}\right) - \bar{p}^{1}_{tot,cell,out}}{\rho(\bar{u}_{z,outlet}(z_{1,begin}))^2/2}. \tag{15}$$

Despite the complexity of the encountered flow patterns, the reduction of such complex, intrinsically 3-dimensional flows to 0-dimensional pressure loss equations is common practice and has been shown to work for a large variety of problems [16]. Through rigorous application of such a methodology to all flow features in the stack, the pressure at these strategically selected positions of the stack can be reconstructed with enough precision to provide a satisfactory prediction of the flow maldistribution, which is shown in Section 3.3.

2.4. Closed-form expressions for pressure losses

In order to compute flow distribution in a manifold with the geometry defined in Section 2.1 using a network model based on the Bernoulli equation, the total pressure losses identified in the previous section need to be estimated as functions of the local flow conditions and geometry. In this study, the number of relevant geometrical factors is minimized by only allowing changes to the number of cells in the stack (and consequently its total height), all other geometric parameters being kept constant.

With the assumption that the loss coefficients in converging and diverging tee junctions can be formulated as a function of the Reynolds number in the common branch Re_C and side branch Re_S as well as the ratio of flow rates between branches (ϱ_{St}/ϱ_C and ϱ_S/ϱ_C), an open source symbolic regression package [28,29] is used to develop expressions for every loss coefficient ζ. Symbolic regression is an application of machine learning which develop analytic functions that model a dataset. In the present case, the loss coefficients ζ_{CS}, ζ_{CSt}, ζ_{SC} and ζ_{StC} determined for the first four simulations listed in Table 3 are used as training data. The aim is to obtain expressions for the loss coefficients that are applicable to a wide range of flow conditions (see Reynolds' law of similarity in Section 2.2) in stacks with a varying amount of cells, provided that the manifold channel width and depth, fuel channel height, inlet and outlet header length, distance between manifold channels and distance between fuel channels is identical. The result of the symbolic regression process is a pareto front composed of a multitude of analytic functions, each representing a different optimum between accuracy of the fit to the training data and complexity of the function. In order to alleviate issues related to overfitting, the fifth simulation case is not used as training data but instead as test data to select an expression that extrapolates correctly beyond the training data. The sixth simulation was not consulted at this stage of the process in order to preserve an unbiased set of validation data.

The same methodology is used to develop analytic expressions for the loss coefficients in the bends at the top of the manifold, although

they are assumed to be only functions of the Reynolds number in the manifold Re_M.

The pressure loss from the inlet to the outlet of a cell was found to be an almost perfectly linear function of the average flow velocity, and therefore the pressure loss can be estimated using Darcy's law for which only the permeability k needs to be determined:

$$\Delta p = \bar{u}\,\frac{\mu\,L}{k}. \tag{16}$$

Herein, this information is used to compute the pressure drop across the cells for the validation of the model which is done by reproducing the flow distribution using the simplified model in Section 3.3. In a full SOC stack model, the difference in pressure across the cells will be influenced by the production and consumption of gas species, which may be computed using adapted flow models [14].

The pressure loss along a straight segment of the manifold (between two gas channels) is commonly computed by evaluating the pressure gradient $\frac{\partial p}{\partial z}$ in a channel using the Darcy–Weisbach equation with conventional Darcy friction factors f_D [13,30–32]:

$$\Delta p = f_D\,L\,\frac{\rho}{2}\,\frac{\bar{u}^2}{D_H}. \tag{17}$$

However, since the flow is not fully developed in any region inside the manifold, the observed pressure gradients deviate strongly from those computed this way (see Section 3.2). So, in order to be able to evaluate the pressure losses in straight segments of the manifold, the pressure gradient is computed using an expression for the Darcy friction factor f_D that is developed using the symbolic regression methodology. The Reynolds numbers in the manifolds and cells (Re_M and Re_{cell}), the ratio of flow rates between branches (Q_{St}/Q_C and Q_S/Q_C) and relative position along the manifold height z/h_{tot} are used as possible variables in the symbolic regression process.

The developed expressions for the pressure loss coefficients and the Darcy friction factors can be found in Section 3.2.

2.5. Network model of the stack flow

The network model developed in this study is an extension of the algorithm of Koh et al. [13] in which five equations are established for each cell in the stack in order to compute the static pressure at the inlet of the diverging tees p^i_{in}, the mass flow rate at the inlet of the diverging tees Q^i_{in}, the mass flow rate through the channels of the cell Q^i_{cell}, the static pressure at the outlet of the converging tees p^i_{out} and the mass flow rate at the outlet of the converging tees Q^i_{out}. The set of $5\,n$ equations for a stack of n cells is formulated as follows:

$$\begin{cases} Q^i_{\mathrm{in}} - Q^i_{\mathrm{cell}} = 0 & i = 1 \\ Q^i_{\mathrm{in}} - Q^{i-1}_{\mathrm{in}} - Q^i_{\mathrm{cell}} = 0 & i \neq 1 \end{cases} \tag{18}$$

$$\begin{cases} Q^i_{\mathrm{out}} - Q^i_{\mathrm{cell}} = 0 & i = 1 \\ Q^i_{\mathrm{out}} - Q^{i-1}_{\mathrm{out}} - Q^i_{\mathrm{cell}} = 0 & i \neq 1 \end{cases} \tag{19}$$

$$\begin{cases} p^i_{\mathrm{tot,in}} + \Delta p^i_{\mathrm{cell}} + \Delta p^i_{\mathrm{B,in}} + \Delta p^i_{\mathrm{B,out}} - p^i_{\mathrm{tot,out}} = 0 & i = 1 \\ p^i_{\mathrm{tot,in}} + \Delta p^i_{\mathrm{cell}} + \Delta p^i_{\mathrm{CS}} + \Delta p^i_{\mathrm{SC}} - p^i_{\mathrm{tot,out}} = 0 & i \neq 1 \end{cases} \tag{20}$$

$$\begin{cases} Q^i_{\mathrm{in}} - Q_{\mathrm{tot}} = 0 & i = n \\ p^{i+1}_{\mathrm{tot,in}} + \Delta p^{i+1}_{\mathrm{W,in}} + \Delta p^{i+1}_{\mathrm{CSt}} - p^i_{\mathrm{tot,in}} = 0 & i \neq n \end{cases} \tag{21}$$

$$\begin{cases} p^i_{\mathrm{tot,out}} - P_0 = 0 & i = n \\ p^i_{\mathrm{tot,out}} - p^{i+1}_{\mathrm{tot,out}} + \Delta p^{i+1}_{\mathrm{W,out}} + \Delta p^{i+1}_{\mathrm{StC}} = 0 & i \neq n \end{cases} \tag{22}$$

with $p_{\mathrm{tot}} = p + \rho\,u^2/2$.

For the purposes of this study, the inlet and outlet of the U-type manifold is assumed to be at the bottom, and the cells are numbered from the top to the bottom. The pressure loss terms Δp are defined as in Sections 2.3–2.4 and computed using the expressions provided in Section 3.2.

The result is a set of nonlinear algebraic equations which can be solved from a reasonable first guess using a damped Newton method.

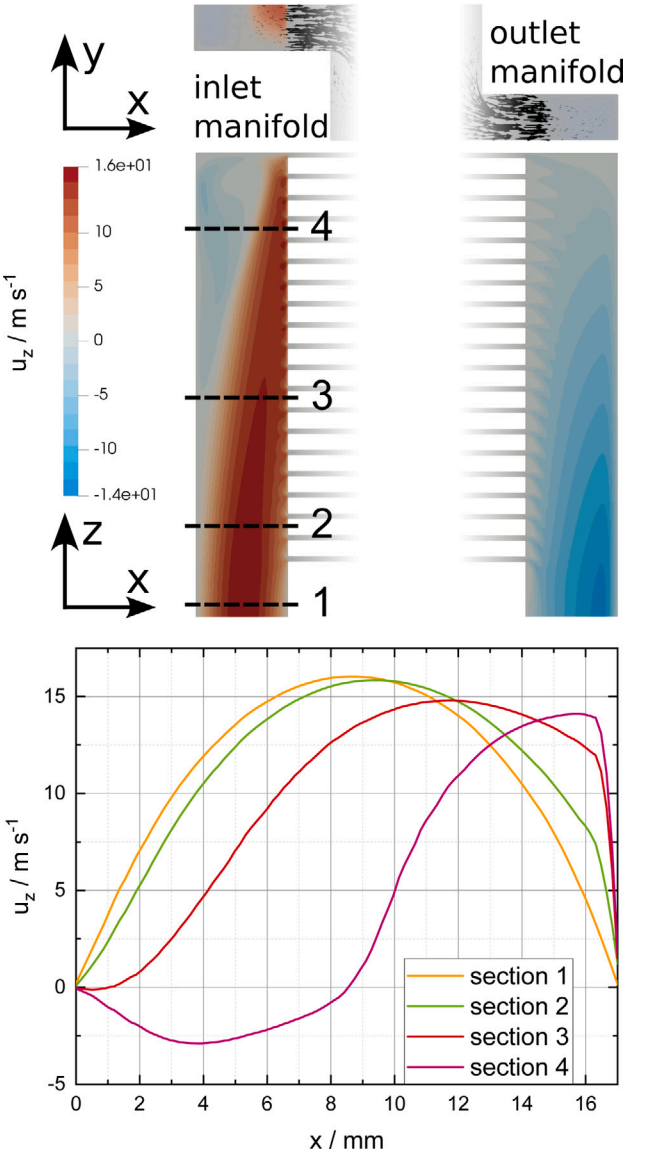

Fig. 4. Axial velocity u_z in the symmetry planes of the inlet and outlet manifolds in the 20 cells $Re_{\mathrm{in}} = 426$ case and profiles of the axial velocity at 4 locations of the inlet manifold. Above the side view of the manifold, a cross-section of the fourth cell is depicted with black arrows showing the velocity vectors in the xy-plane.

3. Results

3.1. Navier–Stokes simulation results

Fig. 4 shows a contour plot of the axial velocity u_z distribution in the symmetry planes of the inlet and outlet manifolds for the simulation with 20 cells and $Re_{\mathrm{in}} = 426$. Additionally, the velocity profiles along four sections of the inlet manifold are depicted.

This visualization shows clearly that the maximum flow velocity in every cross-section of the inlet manifold does not decrease significantly along the length of the manifold, despite the flow rate diminishing greatly between the inlet and the top of the stack. Although the flow rate through Section 4 is 80% lower than the flow rate through Section 1, the maximum velocity decreases by only 12%. At the inlet, the velocity profile is parabolic, as is typical for fully developed channel flows. However, the successive branching of the flow towards the cell channels causes the velocity profile to shift towards one side of the manifold, while a large eddy forms towards the other side.

As a consequence, the velocity gradient at the right side of the channel increases steadily towards the top of the stack, despite the lowering average flow velocity. Since velocity gradients lead to a shearing motion in the flow, the shear stresses (R in Eq. (2)) increase due to the viscosity of the fluid, which is the cause for friction losses. This local increase of the shear stress at the wall is therefore expected to lead to an unusual relationship between flow rate and wall friction losses, which is detailed in the following section.

The flow in the outlet manifold appears to be slightly more homogeneous, although the axial velocity profile is also shifted towards the right. While the wall friction losses are impacted by the skewed velocity profile, the absence of large recirculation zone should facilitate the prediction of pressure losses in the outlet manifold.

3.2. Expressions for the pressure losses

Using the methodology described in Section 2.4, the following expressions were developed for the pressure loss coefficients in the tees and bends:

$$\zeta_{\mathrm{CSt}} = \frac{\overline{p}_{\mathrm{tot,St}} - \overline{p}_{\mathrm{tot,C}}}{\rho \overline{\tilde{u}}^2_{z,\mathrm{C}}/2} \approx 39.67 \left(\frac{Q_{\mathrm{S}}}{Q_{\mathrm{C}}}\right)^2 \frac{Q_{\mathrm{St}}}{Q_{\mathrm{C}}} - 0.4069 \tag{23}$$

$$\zeta_{\mathrm{CS}} = \frac{\overline{p}_{\mathrm{tot,S}} - \overline{p}_{\mathrm{tot,C}}}{\rho \overline{\tilde{u}}^2_{z,\mathrm{C}}/2} \approx -\frac{Q_{\mathrm{S}}/Q_{\mathrm{C}}}{Re_{\mathrm{C}}} \left(226\, Re_{\mathrm{S}} + 3574\right) - 0.9842 \tag{24}$$

$$\zeta_{\mathrm{StC}} = \frac{\overline{p}_{\mathrm{tot,C}} - \overline{p}_{\mathrm{tot,St}}}{\rho \overline{\tilde{u}}^2_{z,\mathrm{C}}/2} \approx \frac{Re_{\mathrm{S}}\, Q_{\mathrm{C}}/Q_{\mathrm{St}} + {}^{15.59}/_{Re_{\mathrm{S}}} - 14.79}{Re_{\mathrm{C}}\, Q_{\mathrm{St}}/Q_{\mathrm{C}}} \tag{25}$$

$$\zeta_{\mathrm{SC}} = \frac{\overline{p}_{\mathrm{tot,C}} - \overline{p}_{\mathrm{tot,S}}}{\rho \overline{\tilde{u}}^2_{z,\mathrm{C}}/2} \approx \frac{2845\, Q_{\mathrm{S}}/Q_{\mathrm{C}}}{1.01 - Re_{\mathrm{C}}} + 0.7872 \tag{26}$$

$$\zeta_{\mathrm{B,in}} = \frac{\overline{p}_{\mathrm{tot,cell,in}} - \overline{p}_{\mathrm{tot,M_{in}}}}{\rho \overline{\tilde{u}}^2_{z,\mathrm{M_{in}}}/2} \approx {}^{-5727}/_{Re_{\mathrm{M_{in}}}} \tag{27}$$

$$\zeta_{\mathrm{B,out}} = \frac{\overline{p}_{\mathrm{tot,M_{out}}} - \overline{p}_{\mathrm{tot,cell,out}}}{\rho \overline{\tilde{u}}^2_{z,\mathrm{M_{out}}}/2} \approx {}^{-4702}/_{Re_{\mathrm{M_{out}}}}. \tag{28}$$

The data points extracted from the first converging and diverging tee from every stack were not used in the symbolic regression of ζ_{CSt}, ζ_{CS}, ζ_{StC} and ζ_{SC}, since a slightly irregular behavior can be expected due to the proximity to the bend at the first cell. In Fig. 5, the selected expressions for converging and diverging tee loss coefficients are plotted against the loss coefficients computed from the OpenFOAM simulation results. The orange markers represent the simulation data that was used to develop the loss coefficients expressions and the magenta markers represent the test data, which was used to verify that the selected expressions extrapolate correctly outside of the calibration range. The green markers represent the validation data, which was only evaluated at the end of the study to provide an unbiased validation case.

Similarly, the selected expressions for inlet and outlet bend loss coefficients are plotted against the loss coefficients computed from the OpenFOAM simulation results in Fig. 6. Contrary to the tees, few data points can be provided since there is only one bend of each type in each simulated case. Fortunately, the close proximity of the data points with similar local Reynolds numbers $\mathrm{Re_M}$ indicates that the pressure loss coefficients in the bends is solely a function of the local Reynolds number and does not depend on the Reynolds number at the inlet of the manifold or the number of cells in the stack.

Normalized root mean square deviations (NRMSD) between the equations and the simulated data, normalized using the range of the simulated data, were computed and listed in Table 4. The NRMSD was selected as a criterion because it emphasizes a good match of every data point by penalizing large errors in single data points (compared, e.g., to an arithmetic average error), while still encouraging a better fit for every data point than using the maximum error as a criterium. The error is normalized to allow for meaningful comparison of the quality of the regression between pressure loss coefficients with large differences in magnitude. The NRMSD is computed by comparing every simulated data point with its counterpart which is computed from the empirical expression by inserting values of Re_{C}, Re_{S}, $Q_{\mathrm{S}}/Q_{\mathrm{C}}$ and $Q_{\mathrm{St}}/Q_{\mathrm{C}}$ found in the simulation for this data point:

$$\mathrm{NRMDS} = \frac{\sqrt{\frac{1}{n_{\mathrm{data}}} \sum_{i=1}^{n_{\mathrm{data}}} \left(\zeta_{\mathrm{sim},i} - \zeta\left(Re_{\mathrm{C}}^{i}, Re_{\mathrm{S}}^{i}, \frac{Q_{\mathrm{S}}}{Q_{\mathrm{C}}}^{i}, \frac{Q_{\mathrm{St}}}{Q_{\mathrm{C}}}^{i}\right)\right)^2}}{\zeta_{\mathrm{sim,max}} - \zeta_{\mathrm{sim,min}}} \tag{29}$$

Excellent agreement is reached for both of the turning loss coefficients ζ_{CS} and ζ_{SC} (NRMSD < 1%), which is of utmost importance as their large magnitude imply a large influence on the flow distribution.

Despite the very simple expressions chosen for $\zeta_{\mathrm{B,in}}$ and $\zeta_{\mathrm{B,out}}$, which is due to the lack of fit data, the agreement of the bend loss coefficients is satisfactory. The impact of this uncertainty on the flow distribution is expected to be moderate because the high magnitude of these loss coefficient is counteracted by the low flow velocities in the corresponding regions. Solely the loss coefficient for the case with the high Reynolds number $Re_{\mathrm{in}} = 426$ is inaccurately predicted, with a NRMSD of 13%.

The expressions obtained for the straight passage loss coefficients ζ_{CSt} and ζ_{StC} are the least accurate, especially ζ_{CSt} for the diverging tees at low Reynolds numbers (see Fig. 5) where the NRMSD reaches 17%. Although the fit could be improved by using expressions with a higher complexity, simplicity is prioritized due to the risk of overfitting and very low magnitude of the corresponding pressure loss and recovery (pressure increase). Since the straight passage pressure loss coefficients are small, the influence on the flow distribution can be expected to be small.

The fact that the fit obtained for pressure losses in the turning flow is more accurate than the fit obtained for the straight passage (considering expressions of similar complexity) is likely due to the fact that pressure losses during flow redirection is mostly caused by friction losses. While the difference in total pressure can be attributed to a single phenomenon in this case, the friction losses for the straight passage are anticipated to be of similar magnitude as the increase in pressure due to the transfer of momentum from the turning flow to the bulk flow, the increase in specific energy due to entrainment of the boundary layer by the turning flow and the disturbance caused by the eddy in the inlet manifold. The straight passage pressure losses being positive or negative depending on the simulated case is likely due to such competing effects.

The expressions developed to compute the Darcy friction factors f_D in straight sections of the inlet and outlet manifolds are listed below:

$$f_{D,\mathrm{in}} \approx \frac{63.13}{Re_{\mathrm{M}}} \left(Re_{\mathrm{cell}} \frac{z}{h_{\mathrm{tot}}} + 0.3544 - \frac{z}{h_{\mathrm{tot}}}\right) \tag{30}$$

$$f_{D,\mathrm{out}} \approx \frac{31.47}{Re_{\mathrm{M}}} \left(Re_{\mathrm{cell}} + 1.4735\right). \tag{31}$$

Table 4
Normalized root mean square deviation between the empirical expressions and the simulated data.

Empirical expression	NRMSD/%		
	Training data	Test data	Validation data
ζ_{CSt}	6.2	7.3	17
ζ_{CS}	0.12	0.18	0.11
ζ_{StC}	2.1	2.2	7.9
ζ_{SC}	0.25	0.79	0.91
$\zeta_{\mathrm{B,in}}$	1.8	13	1.7
$\zeta_{\mathrm{B,out}}$	1.2	1.7	5.2

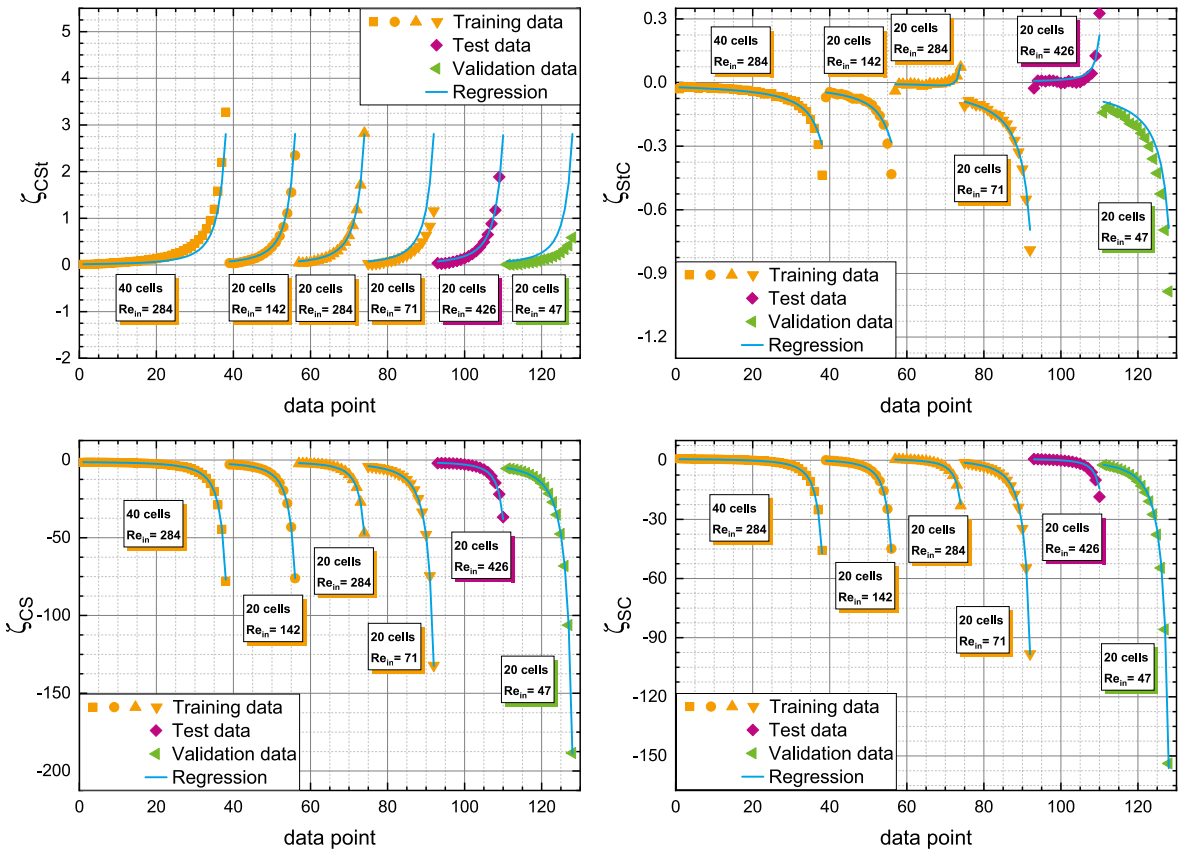

Fig. 5. Pressure loss coefficients in tees computed from detailed simulations (points) plotted against empirical expressions determined through symbolic regression (lines). Each data point corresponds to a single tee, each with a unique combination of Re_C, Re_S, ϱ_S/ϱ_C and ϱ_{Si}/ϱ_C. Data points closer to the top of their respective manifolds feature lower Re_C and ϱ_{Si}/ϱ_C while ϱ_S/ϱ_C grows and Re_S fully depends on the flow distribution. Data points extracted from the same detailed simulations are plotted next to each other. The detailed simulations are described by the number of cells simulated and the Reynolds number at the manifold inlet $\mathrm{Re_{in}}$ (see Table 3).

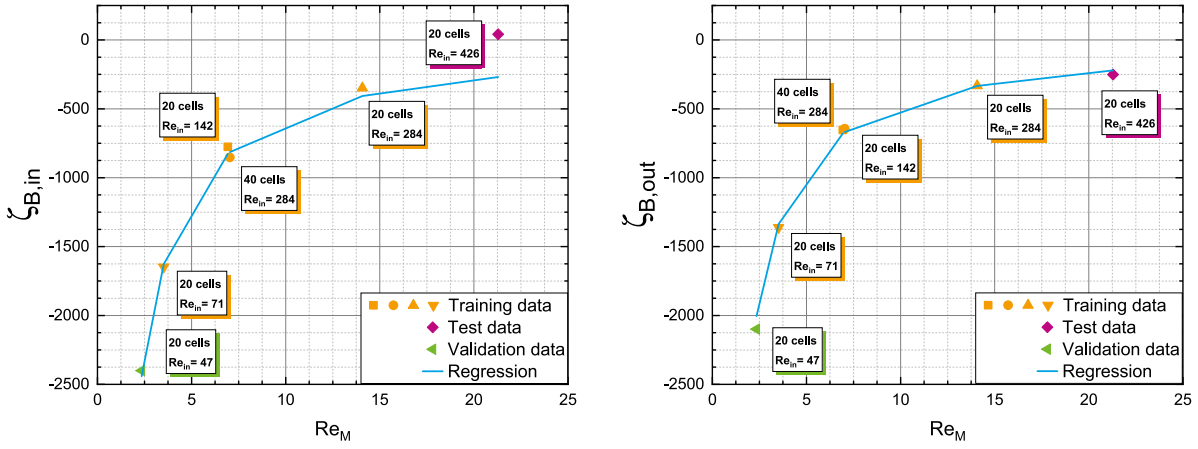

Fig. 6. Pressure loss coefficients in bends computed from detailed simulations (points) plotted against empirical expressions determined through symbolic regression (lines). The abscissa represent the Reynolds numbers $\mathrm{Re_M}$ found at the inlet of the converging bend in the inlet manifold (left) and at the outlet of the diverging bend in the outlet manifold (right). Each data point corresponds to a single bend and is labeled with the simulation it was extracted from (see Table 3).

The pressure gradient in the outlet manifold was observed to be a mostly linear function of the product of the Reynolds number in the manifold Re_M and the Reynolds number in the adjacent cell Re_{cell}, which results in the friction factor $f_{D,out}$ being a linear function of Re_{cell}.

As the considered flow in the manifold channels is laminar, it relates more closely to Darcy's law (Eq. (16)), which predicts a linear growth of the pressure gradient with the velocity. In the present case, the permeability factor k of Darcy's law relates to the aforementioned Darcy friction factors as follows, with D_H being the hydraulic diameter of the manifold:

$$k = \frac{2\,D_H^2}{f_D\,Re_M}. \tag{32}$$

This allows a more straightforward visualization of the parameters influencing the flow in the manifold in Fig. 7. The figure shows that the outlet permeability k_{out} is practically constant for most cases, although

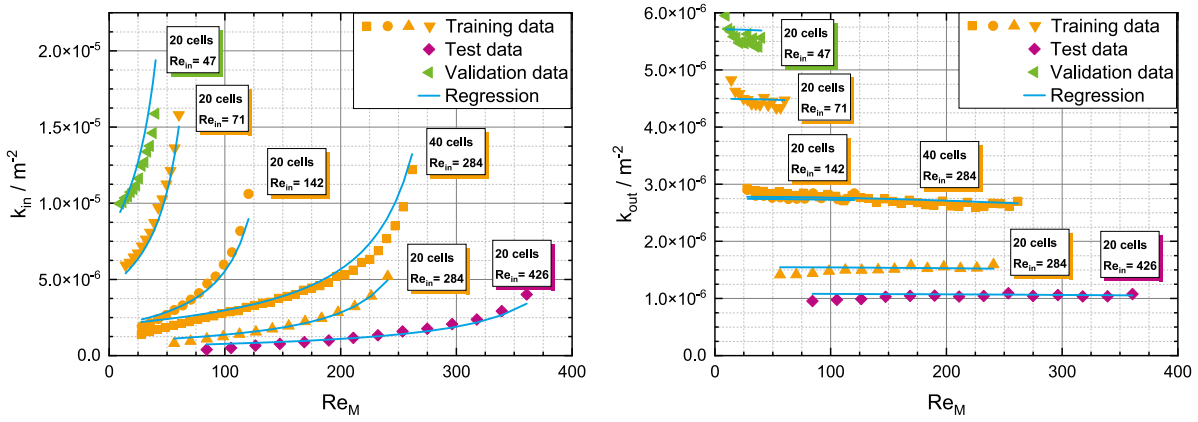

Fig. 7. Permeabilities k of straight sections of the inlet (left) and outlet (right) manifold channels computed from detailed simulations plotted against expressions determined through symbolic regression. The data points are grouped by the simulations they were extracted from, inside of which each point corresponds to a different section of the manifold. The abscissa represent the Reynolds numbers $\mathrm{Re_M}$ found in these sections of the manifold, which is higher close to the inlet of the inlet manifold and close to the outlet of the outlet manifold.

its value changes between the cases. This behavior is a clear contradiction of the commonly assumed Darcy friction factor which is solely proportional to Re_M^{-1} which would manifest as a single horizontal line at $k \approx 1.0 \cdot 10^{-5}$ in these diagrams [33]. Instead, the same permeability is observed for the two cases which feature an identical average flow velocity in the cells of $\bar{u}_{\mathrm{cells}} = 1\,\mathrm{m\,s^{-1}}$, the Reynolds number in the adjacent cells Re_{cell} can be assumed to be a major factor influencing the permeability in the outlet manifold.

The cases with $\mathrm{Re_{in}} = 47$ and $\mathrm{Re_{in}} = 71$ follow a similar trend, although they exhibit an increased permeability by up to 12% at low Reynolds numbers $\mathrm{Re_M}$. In these regions of the flow, the bulk flow in the outlet manifold has very low inertia, resulting in smoother velocity profiles more similar to the fully developed flow which results in lower friction losses. Although the regression does not capture this phenomenon accurately, the low flow velocity relative to the remaining manifold and the small magnitude of the phenomenon implies that the error in the computed pressure difference will be small.

The pressure gradient in the inlet manifold was found to be a non-monotonic function of the Reynolds number in the manifold Re_M, with the pressure gradient increasing from the bottom of the inlet manifold up to half the height of the stack, at which point the maximal pressure gradient is encountered and after which the pressure gradient decreases towards the top of the manifold. This is counter-intuitive, as the highest wall friction losses are expected to be found in the regions with the highest flow rates, which implies that the actual flow maldistribution is greater than might be estimated using pressure gradients for fully developed flow. This behavior is explained by the shape of the velocity profile, which transitions from a parabolic profile at the inlet, to a highly skewed profile in the upper parts of the stack (see Section 3.1). The skewed profile produces high velocity gradients in close proximity to the channel wall adjacent to the inlet headers, which increases the friction losses dramatically. Therefore, the permeability k_{out} attributable to the flow is higher close to the inlet, which is the region with the highest Reynolds number Re_M.

Inside of the cells, in the inlet header, fuel channels and outlet header, the pressure gradient was found to be a perfectly linear function of the flow rate. Sharp total pressure drops occur between those regions due to the sudden change in cross-sectional area, which are located at the inlet and outlet of the headers. These pressure drops are also perfectly linear functions of the flow rate through the cell. Therefore, the pressure drop across a cell can be simplified to a single linear function of the flow rate such as Darcy's law (Eq. (16)), for which the parameter $k = 6.326 \cdot 10^{-8}\,\mathrm{m^2}$ was fitted with a least square method.

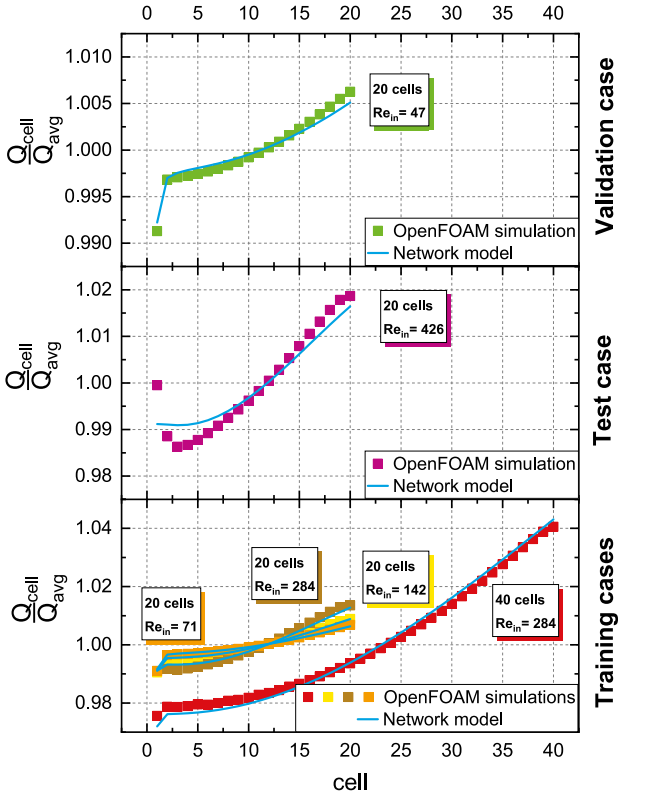

Fig. 8. Flow distribution, represented by the flow rate in every cell normalized by the average flow rate, computed via 3D simulation compared to the network model.

3.3. Flow network model validation

With the expressions for the pressure loss coefficients and pressure gradients listed in the previous section, all pressure losses required in the network model presented in Section 2.5 can be computed. Thereby, the ability of the determined expressions for loss coefficients to predict the flow distribution in the manifold is asserted. The flow distribution computed using the network model are compared to the results of the OpenFOAM simulations in Fig. 8.

Good agreement is reached with every simulation. The largest error is observed for the test case, with $Re_{\mathrm{in}} = 426$, which has a NRMSD for $Q_{\mathrm{cell}}/Q_{\mathrm{avg}}$ of 9.5%. This is due to the relatively high velocity of

the flow which provokes a different flow behavior close to the top of the stack. As the flow stagnates when it reaches the wall at the top of the inlet manifold, the dynamic pressure of the gas, which is its kinetic energy per unit volume, transforms into static pressure. This increases the difference in pressure between the inlet and the outlet of the uppermost cell of the stack, which results in an increased flow rate. While cases with low inlet Reynolds numbers Re_{in} have very sharp drops in flow rates in the uppermost cells due to the increased friction losses in the bend, the effect gradually reverses with increasing Reynolds numbers. In the $Re_{in} = 426$ case, the increased static pressure even reaches the second cell. The overestimated loss coefficient leads to an inability to predict the increased flow rate in the uppermost cell of the stack. Consequently, the accuracy of the predicted flow rates in the remaining cells also suffers, as the local flow conditions are not accurately predicted. Due to the important change in flow distribution caused by this phenomenon, in future model calibrations, the training data should contain a case in which it appears.

The agreement of the model with the remaining simulations, the training cases and the validation case, is excellent, with a NRMSD below 5%. Most of the model inaccuracy is expected to stem from the difficulty in predicting the pressure gradient in the manifold sections close to the inlet, which was explained in the previous section. However, the sudden change in flow rate between the uppermost cells of the stack is predicted with great accuracy in the cases with Reynolds numbers ranging from 47 to 284.

The model developed in this study can therefore be assumed to be accurate inside of this range of Reynolds numbers $Re_{in} \in [47, 284]$. With the considered fuel channel dimensions and fluid properties, in stacks of 20 to 40 cells, this corresponds to average flow velocities in the fuel channels $\overline{u}_{cells}$ of $0.25\,m\,s^{-1}$ to $2\,m\,s^{-1}$, which are commonly encountered. As Reynolds' law of similarity applies, this range can be expressed as $1.3 < Re_{cells} < 10.5$ so that it applies to any Newtonian fluid independently of its density and viscosity.

4. Conclusion

A methodology for the determination of closed-form expressions for the pressure loss coefficients and Darcy friction factors for tee junctions, bends and channels found in SOC stack internal manifolds under laminar flow conditions was presented and used to develop a computationally inexpensive but accurate stack flow model.

Six detailed simulations of the three-dimensional, incompressible flow in a U-Type manifold were performed on a fine mesh for various laminar flow conditions in stacks of 20 to 40 cells. Pressure losses across tees, bends and channels were extracted from all simulations and the pressure loss coefficients and Darcy friction factors corresponding to these losses were evaluated. Pressure losses in the manifold channels were shown to not depend only on the flow velocity, as a linear dependence on the adjacent side channel flow velocity was observed. Additionally, local wall friction losses in the inlet manifold were also shown to change as the parabolic velocity profile found at the manifold inlet transitions to a skewed profile.

After identifying the flow parameters which are most likely to impact the pressure losses in each flow feature, a symbolic regression machine learning algorithm was used to determine functions of those flow parameters which can be used to compute pressure loss coefficients and friction factors for a wide range of flow conditions.

The resulting expressions for the loss coefficients and friction factors were validated by developing a network model of the manifold flow. The system of energy and mass conservation equations supplemented by pressure losses computed with the aforementioned expressions allowed to predict with satisfactory accuracy the flow distribution for two cases which were not used in the development of the model.

The resulting model is fast, with computation times well below one second, and has been designed to be valid for stacks with an arbitrary number of cells and a large range of flow conditions, provided the flow is laminar. The similarity of flows with identical Reynolds numbers also leads the model to be valid for different fluids at different temperatures. Although the loss coefficient and friction factor expressions were developed using simulations of U-type manifolds, the local flow conditions in tees and bends of Z-type manifolds are identical and the newly established expressions can be used to model the flow in such manifolds.

CRediT authorship contribution statement

Oscar Furst: Writing – original draft, Visualization, Validation, Software, Methodology, Investigation. **Olaf Deutschmann:** Writing – review & editing, Supervision, Funding acquisition, Conceptualization.

Declaration of competing interest

The authors declare that they have no known competing financial interests or personal relationships that could have appeared to influence the work reported in this paper.

Data availability

Data will be made available on request.

Acknowledgment

The authors acknowledge support by the state of Baden-Württem berg, Germany through bwHPC. Olaf Deutschmann acknowledges support from Deutsche Forschungsgemeinschaft (DFG) though project DE 659/14-1, project number 460038541. The authors appreciate very fruitful discussions with R.J. Kee (Colorado School of Mines) and J. Daily (EIfER, Karlsuhe).

References

[1] Topsoe to build large-scale SOEC electrolyzer manufacturing facility to meet customer needs for green hydrogen production and SOEC efficiency | Large scale electrolysis, 2021, URL https://www.topsoe.com/press-releases/haldor-topsoe-to-build-soec-electrolyzer-manufacturing-facility. (Accessed 29 November 2023).

[2] Sunfire, Renewable Hydrogen Project "MultiPLHY": World's Largest High-temperature Electrolyzer from Sunfire Successfully Installed, 2023, Sunfire. URL https://www.sunfire.de/en/news/detail/renewable-hydrogen-project-multiplhy-worlds-largest-high-temperature-electrolyzer-from-sunfire-successfully-installed. (Accessed 24 April 2023).

[3] Bloom energy demonstrates hydrogen production with the World's most efficient electrolyzer and largest solid oxide system, 2023, Bloom Energy. URL https://newsroom.bloomenergy.com/news/bloom-energy-demonstrates-hydrogen-production-with-the-worlds-largest-and-most-efficient-solid-oxide-electrolyzer. (Accessed 6 February 2024).

[4] G. Floerchinger, C. Cadigan, N.P. Sullivan, R.J. Braun, Characterizing the performance of kW-scale multi-stack solid oxide fuel cell modules through modeling, ECS Trans. 111 (6) (2023) 803–808, http://dx.doi.org/10.1149/11106.0803ecst, URL https://iopscience.iop.org/article/10.1149/11106.0803ecst.

[5] H. Zhu, R.J. Kee, V.M. Janardhanan, O. Deutschmann, D.G. Goodwin, Modeling Elementary Heterogeneous Chemistry and Electrochemistry in Solid-Oxide Fuel Cells, J. Electrochem. Soc. 152 (12) (2005) A2427, http://dx.doi.org/10.1149/1.2116607, URL https://iopscience.iop.org/article/10.1149/1.2116607.

[6] V. Menon, V.M. Janardhanan, S. Tischer, O. Deutschmann, A novel approach to model the transient behavior of solid-oxide fuel cell stacks, J. Power Sources 214 (2012) 227–238, http://dx.doi.org/10.1016/j.jpowsour.2012.03.114, URL https://www.sciencedirect.com/science/article/pii/S0378775312007902.

[7] M. Mortada, H.S. Ramadan, J. Faraj, A. Faraj, H. El Hage, M. Khaled, Impacts of reactant flow nonuniformity on fuel cell performance and scaling-up: Comprehensive review, critical analysis and potential recommendations, Int. J. Hydrog. Energy 46 (63) (2021) 32161–32191, http://dx.doi.org/10.1016/j.ijhydene.2020.06.013, URL https://linkinghub.elsevier.com/retrieve/pii/S0360319920321492.

[8] Y. Wang, J. Shi, X. Gu, O. Deutschmann, Y. Shi, N. Cai, Toward mobility of solid oxide fuel cells, Prog. Energy Combust. Sci. 102 (2024) 101141, http://dx.doi.org/10.1016/j.pecs.2023.101141, URL https://www.sciencedirect.com/science/article/pii/S0360128523000710.

[9] D.H. Kim, Y. Bae, S. Lee, J.-W. Son, J.H. Shim, J. Hong, Thermal analysis of a 1-kW hydrogen-fueled solid oxide fuel cell stack by three-dimensional numerical simulation, Energy Convers. Manage. 222 (2020) 113213, http://dx.doi.org/10.1016/j.enconman.2020.113213, URL https://linkinghub.elsevier.com/retrieve/pii/S0196890420307573.

[10] R.T. Nishida, S.B. Beale, J.G. Pharoah, L.G.J. de Haart, L. Blum, Three-dimensional computational fluid dynamics modelling and experimental validation of the Jülich Mark-F solid oxide fuel cell stack, J. Power Sources 373 (2018) 203–210, http://dx.doi.org/10.1016/j.jpowsour.2017.10.030, URL https://www.sciencedirect.com/science/article/pii/S0378775317313629.

[11] R.T. Nishida, S.B. Beale, J.G. Pharoah, Comprehensive computational fluid dynamics model of solid oxide fuel cell stacks, Int. J. Hydrog. Energy 41 (45) (2016) 20592–20605, http://dx.doi.org/10.1016/j.ijhydene.2016.05.103, URL https://www.sciencedirect.com/science/article/pii/S036031991530999X.

[12] S.B. Beale, S.V. Zhubrin, A distributed resistance analogy for solid oxide fuel cells, Numer. Heat Transfer B 47 (6) (2005) 573–591, http://dx.doi.org/10.1080/10407790590907930, URL https://www.tandfonline.com/doi/full/10.1080/10407790590907930.

[13] J.-H. Koh, H.-K. Seo, C.G. Lee, Y.-S. Yoo, H.C. Lim, Pressure and flow distribution in internal gas manifolds of a fuel-cell stack, J. Power Sources 115 (1) (2003) 54–65, http://dx.doi.org/10.1016/S0378-7753(02)00615-8, URL https://www.sciencedirect.com/science/article/pii/S0378775302006158.

[14] R.J. Kee, P. Korada, K. Walters, M. Pavol, A generalized model of the flow distribution in channel networks of planar fuel cells, J. Power Sources 109 (1) (2002) 148–159, http://dx.doi.org/10.1016/S0378-7753(02)00090-3, URL https://www.sciencedirect.com/science/article/pii/S0378775302000903.

[15] R. Boersma, N. Sammes, Distribution of gas flow in internally manifolded solid oxide fuel-cell stacks, J. Power Sources 66 (1–2) (1997) 41–45, http://dx.doi.org/10.1016/S0378-7753(96)02469-X, URL https://linkinghub.elsevier.com/retrieve/pii/S037877539602469X.

[16] I.E. Idelchik, Handbook of Hydraulic Resistance, 4th Edition Revised and Augmented, Begell House Inc., 2008, http://dx.doi.org/10.1615/978-1-56700-251-5.0, URL https://www.begellhouse.com/ebook_platform/monograph/book/5877598576b05c67.html.

[17] J.J. Baschuk, X. Li, Modelling of polymer electrolyte membrane fuel cell stacks based on a hydraulic network approach, Int. J. Energy Res. 28 (8) (2004) 697–724, http://dx.doi.org/10.1002/er.993, URL https://onlinelibrary.wiley.com/doi/10.1002/er.993.

[18] L. Wehrle, D. Schmider, J. Dailly, A. Banerjee, O. Deutschmann, Benchmarking solid oxide electrolysis cell-stacks for industrial Power-to-Methane systems via hierarchical multi-scale modelling, Appl. Energy 317 (2022) 119143, http://dx.doi.org/10.1016/j.apenergy.2022.119143, URL https://www.sciencedirect.com/science/article/pii/S0306261922005190.

[19] S.B. Beale, M. Andersson, C. Boigues-Muñoz, H.L. Frandsen, Z. Lin, S.J. McPhail, M. Ni, B. Sundén, A. Weber, A.Z. Weber, Continuum scale modelling and complementary experimentation of solid oxide cells, Prog. Energy Combust. Sci. 85 (2021) 100902, http://dx.doi.org/10.1016/j.pecs.2020.100902, URL https://www.sciencedirect.com/science/article/pii/S036012852030112X.

[20] L. Blum, S.M. Groß, J. Malzbender, U. Pabst, M. Peksen, R. Peters, I.C. Vinke, Investigation of solid oxide fuel cell sealing behavior under stack relevant conditions at Forschungszentrum Jülich, J. Power Sources 196 (17) (2011) 7175–7181, http://dx.doi.org/10.1016/j.jpowsour.2010.09.041, URL https://www.sciencedirect.com/science/article/pii/S0378775310016472.

[21] M. Guo, G. Xiao, J.-q. Wang, Z. Lin, Parametric study of kW-class solid oxide fuel cell stacks fueled by hydrogen and methane with fully multiphysical coupling model, Int. J. Hydrog. Energy 46 (14) (2021) 9488–9502, http://dx.doi.org/10.1016/j.ijhydene.2020.12.092, URL https://linkinghub.elsevier.com/retrieve/pii/S0360319920346577.

[22] L. van Biert, M. Godjevac, K. Visser, P.V. Aravind, Dynamic modelling of a direct internal reforming solid oxide fuel cell stack based on single cell experiments, Appl. Energy 250 (2019) 976–990, http://dx.doi.org/10.1016/j.apenergy.2019.05.053, URL https://www.sciencedirect.com/science/article/pii/S0306261919309079.

[23] M. Preininger, B. Stoeckl, V. Subotic, R. Schauperl, C. Hochenauer, Electrochemical characterization and performance assessment of SOC stacks in electrolysis mode, ECS Trans. 91 (1) (2019) 2589–2600, http://dx.doi.org/10.1149/09101.2589ecst, URL https://iopscience.iop.org/article/10.1149/09101.2589ecst.

[24] K. Kendall, M. Kendall, High-Temperature Solid Oxide Fuel Cells for the 21st Century: Fundamentals, Design and Applications, Academic Press is an imprint of Elsevier, London, 2016.

[25] OpenFOAM | Free CFD Software | The OpenFOAM Foundation, 2024, URL https://openfoam.org/. (Accessed 26 February 2024).

[26] OpenFOAM: User Guide: simpleFoam. URL https://www.openfoam.com/documentation/guides/latest/doc/guide-applications-solvers-incompressible-simpleFoam.html.

[27] P.J. Roache, Perspective: A method for uniform reporting of grid refinement studies, J. Fluids Eng. 116 (3) (1994) 405–413, http://dx.doi.org/10.1115/1.2910291, URL https://asmedigitalcollection.asme.org/fluidsengineering/article/116/3/405/411554/Perspective-A-Method-for-Uniform-Reporting-of-Grid.

[28] D. Segal, SymbolicRegression Julia Package, 2023, URL https://juliapackages.com/p/symbolicregression. (Accessed 4 December 2023).

[29] M. Cranmer, Interpretable Machine Learning for Science with PySR and SymbolicRegression.jl, 2023, http://dx.doi.org/10.48550/arXiv.2305.01582, arXiv [astro-ph, physics:physics] URL http://arxiv.org/abs/2305.01582.

[30] Y. Qin, G. Liu, Y. Chang, Q. Du, Modeling and design of PEM fuel cell stack based on a flow network method, Appl. Therm. Eng. 144 (2018) 411–423, http://dx.doi.org/10.1016/j.applthermaleng.2018.08.050, URL https://www.sciencedirect.com/science/article/pii/S1359431118306070.

[31] J. Wang, Theory of flow distribution in manifolds, Chem. Eng. J. 168 (3) (2011) 1331–1345, http://dx.doi.org/10.1016/j.cej.2011.02.050, URL https://www.sciencedirect.com/science/article/pii/S1385894711002300.

[32] G. Karimi, J.J. Baschuk, X. Li, Performance analysis and optimization of PEM fuel cell stacks using flow network approach, J. Power Sources 147 (1) (2005) 162–177, http://dx.doi.org/10.1016/j.jpowsour.2005.01.023, URL https://www.sciencedirect.com/science/article/pii/S0378775305001539.

[33] H. Bruus, Theoretical microfluidics, Oxford Master Series in Physics, (18) Oxford University Press, Oxford ; New York, 2008, oCLC: ocn156817008.